Title

Contributions to the dielectric losses of textured SrTiO3 thin films with Pt electrodes

Journal

Journal of Applied Physics, 98

Authors

Lu, Jiwei
Schmidt, Steffen
Ok, Young-Woo
et al.

Publication Date

2005

Peer reviewed

Contributions to the dielectric losses of textured $SrTiO_3$ thin films with Pt electrodes

Jiwei Lu, Steffen Schmidt, Young-Woo Ok[a)], Sean P. Keane and Susanne Stemmer[b)]

Materials Department, University of California, Santa Barbara, CA 93106-5050

[a)] Current address: Department of Materials Science and Engineering, Gwangju Institute of Science and Technology (GIST), Gwangju 500-712, Korea

[b)] Electronic mail: stemmer@mrl.ucsb.edu

Abstract

The factors controlling low frequency (1 MHz) dielectric losses of textured $SrTiO_3$ thin films deposited by radio-frequency magnetron sputtering on platinized sapphire substrates were investigated. In particular, the influence of film texture, phase transformations, applied bias field, temperature and annealing atmospheres was studied. Films that were (111) textured showed a phase transformation at ~ 150 K, whereas films that were predominantly (110) oriented did not exhibit a phase transformation in the measured temperature range (100 K – 300 K). Two major contributions to the dielectric losses were identified: a low temperature loss increase for the (111) oriented film, which could be suppressed by an applied bias field, and a loss peak at ~ 250 K (at 1 MHz), which was strongly frequency dependent and likely associated with a relaxing defect. The low temperature loss mode was related to the appearance of a phase transformation and contributed to the dielectric losses even at temperatures that were more than 100 K above the phase transformation. In contrast to the leakage properties of the films, which were strongly dependent on annealing atmospheres, annealing under reducing conditions had no significant influence on any of the observed loss modes. Possible origins of the different loss contributions are discussed.

I. INTRODUCTION

Ferroelectric or incipient ferroelectric oxides with the perovskite structure, such as $SrTiO_3$ and $(Ba,Sr)TiO_3$ (BST) that exhibit a nonlinear, electric field tunable dielectric permittivity are of interest for tunable microwave devices such as phase shifters and filters [1]. The relative dielectric tunability is defined as $n_r = [\varepsilon(0) - \varepsilon(E)]/\varepsilon(0)$, where $\varepsilon(0)$ is the zero field dielectric permittivity and $\varepsilon(E)$ is the permittivity under an applied electric field E. For microwave applications films are used in their paraelectric phase. The largest dielectric tunabilities are achieved close to the paraelectric/ferroelectric phase transformation temperature [2].

Wide spread application of ferroelectric thin films in tunable microwave devices has thus far not been realized, due to unacceptably high dielectric losses in thin films. At lower frequencies, extrinsic losses, such as due to point defects, local polar regions and a poorly understood universal relaxation mechanism, are thought to dominate, whereas at microwave frequencies, losses are believed to be both extrinsic and intrinsic in origin [1]. Intrinsic losses are due to the interaction of phonons with the AC measuring field, and several different mechanisms may be active [1,3,4]. Identification of the dominant loss mechanisms in thin films at microwave frequencies is often complicated due to contributions from electrodes, which may dominate the loss characteristics of devices at high frequencies [5,6]. Recently, several authors have proposed to use the bias field dependence of the dielectric loss as a method to distinguish between different loss mechanisms [7,8].

The goal of this paper is to study the contributions to the dielectric losses in thin films with well-characterized microstructures. We will focus on low-frequency (1 MHz) dielectric properties, as an initial step towards understanding the high-frequency properties. All studies

were carried out using Pt/$SrTiO_3$/Pt parallel plate capacitor structures. Pt has a high chemical and thermal stability as well as a high electrical conductivity, required for microwave applications. $SrTiO_3$ is a prototypical soft-mode incipient ferroelectric with the perovskite structure and is one of the most extensively characterized complex oxides [9-12]. At low temperatures, $SrTiO_3$ shows a nonlinear, electric field tunable dielectric permittivity, which is of interest for tunable microwave devices operating at cryogenic temperatures. At ~ 105 K, bulk $SrTiO_3$ undergoes a structural (but not ferroelectric) phase transition to a tetragonal phase, which is accompanied by a soft mode [10-12]. Above this phase transformation, the dielectric permittivity follows a Curie-Weiss type law with a Curie-Weiss temperature of ~ 35 K [13]. $SrTiO_3$ thin films are also of interest as a model system for other tunable dielectric thin films such as BST, because properties can be studied over a wide temperature range, without the possible influence of inhomogeneities in the A-site cation distribution.

II. EXPERIMENTAL

100 nm thick Pt electrodes were deposited on *c*-plane sapphire by DC sputtering at a substrate temperature of 650 °C or by electron beam evaporation with no intentional heating of the substrate, respectively. Substrates for the electron beam evaporated Pt electrodes were covered with ~ 3 nm thick e-beam Ti adhesion layers, which significantly affected the texture of the $SrTiO_3$ films subsequently grown onto them, as described below. As reported elsewhere [14-16], both methods yielded Pt films with orientation relationships characterized by $(111)_{Pt} \| (0001)_{Al_2O_3}$ and $[01\bar{1}]_{Pt} \| [10\bar{1}0]_{Al_2O_3}$. The epitaxial Pt films showed rotational twinning [14,15,17].

Approximately 100 nm thick $SrTiO_3$ thin films were grown by radio-frequency (rf) magnetron sputtering, concurrently on both types of electrodes. Rutherford backscattering spectroscopy (RBS) in combination with electrical measurements was used to optimize the growth conditions (Table I) for cation stoichiometry and low dielectric losses. X-ray diffraction (XRD) was used to analyze the film textures. The surface morphology and film thickness (after patterning) were characterized by atomic force microscopy (AFM). Secondary ion mass spectrometry (SIMS) with a Cs ion beam (Physical Electronics PHI 6650) was used to identify the impurities in the films. The extended defect structure of the films was characterized by transmission electron microscopy (TEM) using a conventional TEM (Tecnai G2 Sphera) operated at 200 kV. Plan-view TEM samples were prepared by standard techniques from larger patterns without top electrodes located on the same wafers as the capacitor structures used for electrical characterization.

Parallel plate capacitor structures for dielectric characterization were fabricated in a two-step mask process. The first mask defined the active dielectric area. $SrTiO_3$ films were patterned using diluted HF (1:1). The second mask was used to pattern 200 nm thick, electron-beam evaporated Pt top contacts by a lift-off process. After patterning of the top electrodes, a rapid thermal annealing treatment was performed at 700 ºC in ultra-high purity nitrogen for 30 seconds, which significantly improved the dielectric loss behavior. This capacitor will be referred to as “as-fabricated”.

Unless stated otherwise, the dielectric properties were characterized at 1 MHz with a 500 mV oscillation voltage using an impedance analyzer (Agilent model 4294A) connected to air coplanar probes (Cascade Microtech, Inc.). Temperature dependent measurements (100 K - 300 K) were performed using a cryogenic wafer probe station (RMC Cryosystems). The out-of-plane

dielectric constants (ε_r) and out-of-plane dielectric susceptibility χ_{33} were calculated from the measured device capacitance (C_{device}) of 50 μm × 30 μm top electrodes, i.e. $\varepsilon_r = C_{device} \cdot t / A \cdot \varepsilon_0$ and $\varepsilon_r = 1 + \chi_{33} / \varepsilon_0$ where t is the $SrTiO_3$ film thickness determined by AFM, ε_0 the permittivity of free space and A the capacitor area. Dielectric loss tangents ($\tan \delta$) were calculated from the measured device quality factor Q, i.e. $\tan \delta = Q^{-1}$. Leakage currents of 150 μm × 130 μm capacitors were measured using a HP 4155 Semiconductor Parameter Analyzer using 0.05 V steps with a one second delay per step. The polarization as a function of applied field was measured in virtual ground mode with a Radiant ferroelectric test system (RT66A) attached to a probe station with a Joule-Thompson refrigerator (MMR).

The dielectric properties of the capacitors were characterized before and after annealing treatments of the fabricated devices in different atmospheres. The first annealing was carried out in vacuum (~ 10^{-7} Torr) at ~ 700 °C (substrate temperature) for 30 minutes in the sputter chamber. The second annealing treatment was carried out in air in a tube furnace at 700 °C for 30 minutes. The ramp up/down time for all annealing and growth experiments was 10 K/min.

III. RESULTS AND DISCUSSION

A. $SrTiO_3$ thin film microstructure

The microstructure of $SrTiO_3$ films on sputtered Pt electrodes (no Ti underlayer) has been described in detail in a previous publication [15]. Very briefly, these films contained both (111) and (110) oriented grains, with an area ratio of approximately 1:3 [15]. Figures 1 and 2(a) show XRD spectra and an AFM image of this film, respectively. The elongated grains in the AFM image were (110) textured grains [15], whereas the more equiaxed grains were of either (110) or

(111) texture. Some (100) oriented grains could also be detected in XRD. In contrast, the $SrTiO_3$ films grown on the electron beam evaporated Pt with Ti adhesion layers contained mostly (111) oriented grains, as was confirmed by plan-view TEM studies that will be reported elsewhere [16]. The (111) peaks of $SrTiO_3$ in the XRD spectra (Fig. 1) could not be resolved due to the strong signal from the (111) oriented Pt film and the close match in lattice parameters (at room temperature the lattice mismatch was 0.4%). XRD scans also showed some unidentified peaks (Fig. 1). AFM of this film [Fig. 2(b)] showed triangular shaped grains due to strong surface faceting. The surface roughness (root mean square, RMS) of the films was ~ 4.7 nm for (110)/(111) textured film on sputtered Pt and ~ 8.4 nm for the (111) textured film. The greater RMS values of the (111) textured film were mainly due to the surface faceting of the (111) grains [16]. AFM of unpatterned (111) $SrTiO_3$ oriented films without top-electrodes showed that the grain size of the films increased after annealing in vacuum (from ~ 75 nm to ~ 90 nm).

Plan-view TEM showed that the orientation relationship between the (111) oriented grains and Pt could be described by $[111]_{SrTiO_3} \| [111]_{Pt}$ and $\{\bar{1}10\}_{SrTiO_3} \| \{\bar{1}10\}_{Pt}$ with two twin related orientation variants forming twin boundaries labeled "T" in Fig. 3. Plan-view transmission electron microscopy (Fig. 3) showed that the density of threading dislocations (labeled "O" and "A" in Fig. 3) was in the order of $5\square10^{10}$ /cm^2.

SIMS showed that the Pt electrodes on the Ti adhesion layers contained Ti, consistent with findings by others [18-20]. The influence of Ti underneath (111) textured Pt electrodes on perovskite film texture is well documented [21,22]. For example, Tani *et al.* reported a change from (100) to (111) texture in $Pb(Zr,Ti)O_3$ thin films, if Ti from the adhesion layer migrated to the electrode surface [22]. Further studies are necessary to identify the mechanism that induced

such a strong preference for (111) $SrTiO_3$ film texture. Nevertheless, the two films with different orientations allowed for the characterization of the dielectric properties as a function of film texture independently of their defect chemistry, which in two simultaneously deposited films should be similar.

B. Room temperature dielectric properties of films with different texture

Table II summarizes the room temperature dielectric properties of the (111) and (110)/(111) textured $SrTiO_3$ thin films under zero applied bias field before and after the different annealing treatments. All measurements were done on the same device; therefore, observed changes were not due to variations between devices.

Both the permittivity and the dielectric loss tangent of the (111) oriented $SrTiO_3$ film were greater than those of the (110)/(111) textured film. The greater permittivity of the (111) oriented film was consistent with our previous estimates obtained from Landau-Ginzburg-Devonshire models [15]. These models predicted that in the paraelectric phase, the permittivity of a (111) oriented $SrTiO_3$ film that is under biaxial tensile strain due to the thermal mismatch with the substrate is greater than that of a (110) oriented film [15]. $SrTiO_3$ films on sapphire substrates were under biaxial tension after cooling from the deposition because the thermal expansion coefficient of $SrTiO_3$ ($\alpha_{SrTiO_3} = 10 \times 10^{-6}$ K^{-1} [23]) was greater than that of sapphire ($\alpha_{Al_2O_3} = 7 \times 10^{-6}$ K^{-1} [24]).

After each annealing step the dielectric constant of both films increased, independent of the annealing atmosphere. The increase in permittivity was likely due to a reduction in extended defect density (for example an increase in grain size) with annealing, which resulted in a greater dielectric polarizability of the films. In contrast, there was no detectable change in the zero-bias

loss tangents with annealing in either a reducing (vacuum) or oxidizing (air) atmosphere. Since dielectric losses were expected to be sensitive to the point defect chemistry, two possible explanations could be suggested: *(i)* the annealing conditions did not produce any changes in the defect chemistry of the films or *(ii)* the zero-bias loss tangent was not sensitive to any defects whose concentration may be affected by vacuum or air annealing. To distinguish between these two possibilities the dielectric properties were measured as a function of temperature (section C) and as a function of applied DC bias field.

Figure 4 shows the permittivity and dielectric loss tangent as a function of applied field for the two films for positive bias voltages for the different annealing conditions. The films showed a moderate dielectric tunability of about 30% at room temperature. At low fields, the dielectric loss of the (110)/(111) oriented film was essentially independent of bias field [Fig. 4(b)], whereas the (111) oriented field showed a slight decrease in loss with increase in bias field [Fig. 4(a)]. This will be discussed further below. No changes were observed in the dielectric loss up to relatively high bias fields with annealing in different atmospheres. At high bias fields (> 350 kV/cm), the vacuum anneal caused the dielectric loss to increase steeply at high applied fields for both films. Subsequent annealing in an oxygen-rich atmosphere (air) caused the dielectric losses to return to their values measured before the vacuum anneal.

Figure 5 shows that the increase in loss at high fields after vacuum annealing was correlated with charge injection from the electrodes at high fields and was *not* due to an intrinsic characteristic of the dielectric itself. This was evident from a comparison of the field dependence of the DC leakage current and dielectric losses for the (110)/(111) oriented film after vacuum and air annealing, respectively (measured on two different devices), shown in Fig. 5. The behavior at negative bias voltages was similar, except that the steep loss increase occurred at

lower fields for the vacuum annealed capacitors compared to positive bias. This may be due to differences in the barrier properties of the bottom and top electrodes, and requires further studies. After vacuum annealing, the leakage current and loss characteristics were severely degraded, but subsequent annealing in air recovered the as-fabricated leakage properties, consistent with the loss behavior. The high-field leakage in $Pt/SrTiO_3/Pt$ capacitors is known to be controlled by thermionic emission over the Schottky barriers at the electrode interfaces [25-28], with the current density J given by [26]:

$$J = A^* T^2 \exp\left(\beta E^{1/2} - \phi_B / kT\right); \quad \beta = \left(q^3 / 4\pi\varepsilon\varepsilon_0\right)^{1/2} \tag{1}$$

where A^* is the Richardson constant, E the applied field, T the temperature, ϕ_B the barrier height, q the elementary charge and k the Boltzmann constant. By plotting ln J against $E^{1/2}$ at a constant temperature straight lines were expected. The inset in Fig. 5 showed that the lines were parallel before and after annealing in air, indicating that all parameters in Eq. (1) except the barrier height were the same. The change in barrier height was estimated to be about ~ 0.24 eV.

In the literature, it has been shown that leakage characteristics and Schottky barrier heights in Pt/perovskite structures are sensitive to annealing and deposition conditions [27,29-32]. In particular, it has been established that oxygen anneals reduced high field leakage, whereas forming gas (hydrogen) anneals increased high-field leakage in $SrTiO_3$ and BST films with Pt electrodes. For non-ideal Schottky barriers, interface states, deep level traps, space charges and fixed interface charge determine the effective interfacial barrier height and could all be influenced by annealing conditions [29]. Given that the degradation of high-field leakage and loss behavior after vacuum anneals could be reversed by annealing under high oxygen partial pressure (air), the effective barrier height was likely related to the oxygen vacancy concentration.

Under the experimental conditions, no kinetic limitations to oxygen exchange with the atmosphere were believed to exist [33]. While oxygen can diffuse through Pt electrodes [34], it should be noted that the $SrTiO_3$ films were patterned, thus facilitating exchange with the atmosphere. The Pt electrodes may also promote catalytic effects [35].

In addition to oxygen vacancies, the influence of hydrogen should be considered, because oxygen vacancies and hydrogen may have similar effects on leakage properties [30]. More recently, however, it has been argued that deuterium produces only electrically inactive defects in BST [36]. If the observed effective barrier lowering was due to hydrogen, this would imply that hydrogen was introduced during the vacuum anneal and removed in the furnace anneal. SIMS (Fig. 6) showed that the films contained hydrogen, but no difference in the bulk concentration could be detected between films annealed in vacuum and in air, respectively (the hydrogen peaks at the interfaces were due to an increase in ion yield at the interface [37]). In the literature, it was shown that both oxygen and vacuum anneals removed deuterium from BST films [30]. Thus, it seemed more likely that the increase in loss at higher fields after vacuum anneals was due to an effective lowering of the Schottky barrier height associated with the formation of oxygen vacancies. Defects introduced by vacuum annealing did, however, not influence the dielectric losses at zero to intermediate bias fields. Thus, to further investigate the factors that controlled the dielectric losses not determined by charge injection from the electrodes, temperature dependent dielectric studies were carried out.

C. Dielectric behavior of $SrTiO_3$ thin films as a function of temperature

Figure 7 shows the inverse dielectric susceptibility for the two films with different texture as a function of temperature between 100 K and 300 K. Consistent with our predictions for

(111) oriented films under biaxial tensile stress, the (111) film showed a greater out-of-plane dielectric permittivity over the entire temperature range [15]. In the cubic phase, the inverse susceptibility of $SrTiO_3$ should follow a Curie-Weiss law: $\varepsilon^{-1} = C/(T - T_c)$, where C is the Curie-Weiss constant and T_c the Curie-Weiss temperature. Fitting the data to a Curie-Weiss law (Fig. 7) yielded negative values for T_c. This was due to a thickness effect that could be described by a low permittivity interfacial layer connected in series with the bulk of the film [38,39]. Removing this thickness effect resulted in positive T_c values, as shown elsewhere [15]. A deviation from the linear Curie-Weiss behavior can clearly be seen for the (111) textured film below ~ 150 K, indicating that the films underwent a phase transformation. In contrast, the (110)/(111) oriented film did not show a deviation from linear behavior in the measured temperature range. Measurements of ferroelectric hysteresis curves of the (111) oriented film showed linear dielectric behavior at room temperature and loops with a very small remanent polarization at 80 K, indicating that this phase transformation was ferroelectric in nature, rather than purely structural. Shifts in phase transformation temperatures were expected from thermodynamic theory for epitaxial perovskite films under biaxial strain [40,41]. For (001) oriented epitaxial $SrTiO_3$ thin films, such models predict both purely structural and ferroelectric phase transformations in the measured temperature range even for moderate biaxial stresses [42]. In the literature, ferroelectric phase transformations have been reported for (001) oriented $SrTiO_3$ thin films at temperatures above 100 K [43-45]. To predict the appearance of ferroelectricity and/or shifts in the structural phase transformation temperatures for (111) and (110) oriented films, modifications of these models are currently underway and a quantitative comparison with the experimental data on differently oriented films will be subject of a forthcoming study [46].

Figure 8 shows the dielectric loss at zero applied bias field for the two films as a function of temperature and annealing treatment. Consistent with the data at room temperature, annealing under reducing or oxidizing conditions did not influence the losses at zero applied field at any temperature. All samples showed a dielectric loss peak around 250 K at 1 MHz (arrows in Fig. 8). The temperature of the maximum of this loss peak (T_m) was strongly dependent on the measurement frequency (see Fig. 9). Fitting the frequency (f) versus T_m data to an Arrhenius equation $f = f_0 \exp(-E_a / kT_m)$, where E_a is the activation energy and f_0 is the attempt jump frequency, gave E_a = 0.29 eV and $f_0 = 6 \times 10^{11}$ Hz. At low temperatures, the two differently oriented films showed a markedly different loss behavior. For the (111) oriented film [Fig. 8 (a)], losses increased sharply at temperatures approaching the phase transition. In contrast to the loss peak at 250 K, the onset of the low temperature loss mode appeared to be essentially independent of the measurement frequency (see Fig. 9). For the (110)/(111) oriented film, only a slight increase in loss at lower temperatures was observed [Fig. 8 (b)]. The minimum loss tangent for the (110)/(111) film was around 0.0015, which was higher than that of single crystals, in which the lowest reported losses were around 2×10^{-4} [47-49].

Figure 10 shows the temperature dependence of the dielectric losses under an intermediate bias field (E ~ 300 kV/cm) as a function of annealing. The loss peak at 250 K was not affected by an applied bias field or by the annealing atmosphere. In contrast, the applied bias field strongly influenced the low temperature loss mode of the (111) film that was observed under zero bias, which was almost completely suppressed. The electric field also reduced the loss of the (110)/(111) film at the lowest temperatures.

The temperature dependence of the dielectric losses under a large electric field (E ~ 500 kV/cm) is shown in Fig. 11. At these very high fields, the loss mode around 250 K appeared

suppressed. Consistent with the data measured at room temperature, the losses at high fields increased after the vacuum anneal. The increase was reversible by subsequent annealing in air at all temperatures for the (111) oriented film, whereas the (110)/(111) oriented film did not show complete reversibility at low temperatures. The (110)/(111) oriented film annealed in vacuum showed a somewhat more complicated behavior with first an increase and then a large decrease in loss at the lowest temperatures. As shown above, loss at high fields was correlated with leakage across the Schottky barrier. The increase in loss (leakage) with decreasing temperature resembled a recently reported positive resistance behavior at high fields in BST films [50]. The results showed that the behavior may be connected to a point defect in the film and specific properties of the interface, as it was not observed in the as-deposited films or in the (111) oriented film.

To summarize the experimental results, two major contributions to the losses in sputtered, highly textured $SrTiO_3$ thin films were identified in this study. These two contributions showed very different characteristics as a function measurement frequency and applied electric field: a low temperature loss increase that occurred only in the (111) oriented film, and which could be suppressed by an applied bias field, and a loss peak in both films at about 250 K (at 1 MHz), which was strongly frequency dependent. We next discuss the possible origins for the observed loss contributions.

The low temperature loss mode observed only for the (111) oriented film was correlated with a – likely strain induced – phase transformation at ~ 150 K and was responsible for the differences in the dielectric loss behavior of the (111) and the (110)/(111) oriented films, respectively. The two films were deposited simultaneously; thus their point defect chemistry was likely very similar. It should thus be emphasized that the apparent orientation dependence

of the magnitude of the loss measured for the two differently oriented films is an indirect effect that is related to the different mechanical boundary conditions (and possibly different magnitudes of film strain) that induce a phase transformation in the (111) oriented film, rather than an intrinsic anisotropy of the dielectric loss itself. Ferroelectric materials typically show an increase in loss near the ferroelectric phase transformation temperature [51]. Even in perfect crystals, polarization fluctuations are believed to contribute to the dielectric loss and become large near the phase transition temperature [4,51]. The absence of a strong frequency dependence of the *onset* temperature of this loss mode made it unlikely that it was related to ferroelastic domain wall relaxations, as suggested in the literature for $SrTiO_3$ single crystals [52]. The contribution to the dielectric loss due to this mechanism decreased with increasing temperature and was also strongly dependent on the applied electric field [see Figs. 8 (a) and 10 (a)]. Even at room temperature, i.e. more than 100 K above the phase transformation, this loss mechanism caused the loss of the (111) oriented film to be higher than that of the predominantly (110) oriented film. This was evident from Fig. 4(a)), which showed that at room temperature, the (111) oriented film not only showed higher loss but also a slight decrease in loss under a small applied field, which is a characteristic feature of the loss mechanism associated with the phase transformation. It should be noted that an electric field dependence of the loss has also been observed for other paraelectric, tunable thin films, such as BST [53,54]. The results in this study correlated this behavior with the proximity to a ferroelectric phase transformation. Future experimental studies should be directed towards establishing the frequency dependence of the *magnitude* of this loss, in particular in the microwave frequency region.

In contrast, the temperature of the maximum of the second loss mechanism (loss peak at ~ 250 K at 1 MHz) was strongly frequency dependent and thus likely due to a dipolar relaxation

[55]. A peak at 165-175 K at 10 kHz, albeit with a somewhat smaller activation energy has been observed by other authors in laser-ablated $SrTiO_3$ thin films, who suggested that it was due to oxygen vacancies [56,57]. Not consistent with this interpretation, Fig. 8 showed that annealing under vacuum or air did not affect this loss peak. Many other defects besides oxygen vacancies may exist in films deposited by high energetic deposition processes from ceramic targets (such as laser ablation and sputtering), including defects on the cation sites as well as unintentional impurities from the target or the electrodes. This loss mode was independent of the film orientation, indicating that it was likely not due to an extended defect (such as grain boundaries), which were somewhat different in the two films. Further studies are needed to determine the precise point defect chemistry of these films to establish a direct relationship to this loss mechanism.

IV. CONCLUSIONS

Studies of the dielectric loss and permittivity of textured $SrTiO_3$ thin films as a function of temperature, bias field, annealing conditions and film orientation provided insights into the contributions to dielectric loss of paraelectric, sputtered $SrTiO_3$ thin films. In particular, we have shown:

(1) In contrast to predominantly (110) oriented films, the permittivity of (111) oriented $SrTiO_3$ films that were under a tensile biaxial stress due to the thermal mismatch with the substrate showed a deviation from the linear Curie-Weiss behavior at about 150 K due to a phase transformation that is likely ferroelectric in nature. High temperature anneals, independent of the annealing atmosphere, increased the permittivity of the films.

(2) Even at temperatures far above the phase transformation temperature, losses at zero bias field of (111) oriented films were dominated by a loss mechanism that was associated with the phase transformation and that caused a steep increase in loss for temperatures approaching the phase transformation. This loss mode could be suppressed by an applied electric field.

(3) In these films, high dielectric tunabilities will invariably be associated with high dielectric losses under zero bias field, as both tunability and losses increased with the proximity to the phase transformation temperature.

(4) The results showed that film strain may have an indirect effect on dielectric losses by shifting or inducing ferroelectric phase transitions. Studies that observe a change in dielectric losses with annealing should carefully distinguish between several possible explanations that may all be associated with a decrease in loss. These include a shift in a ferroelectric phase transformation temperature (for example due to a change in film strain or extended defect density due to the annealing) and the reduction in the contribution of an extrinsic loss mechanism (such as point defects).

(5) All films showed a strongly frequency dependent loss mode not found in single crystals, which occurred at ~ 250 K at 1 MHz and which showed the characteristics of a relaxing defect. As with the loss mode at low temperatures, annealing in vacuum did not affect this loss peak, thus it was likely not due to oxygen vacancies. In contrast to the low temperature loss mechanism associated with the phase transformation, an applied electric field only weakly influenced this loss peak.

(6) Although often cited in the literature as a possible reason for high losses in perovskite thin films [56,58-60], the results in this study showed that oxygen vacancies are likely not

responsible for high extrinsic dielectric losses in sputtered $SrTiO_3$ thin films in the measured frequency range. These observations are consistent with experiments on single crystals that have shown long ago that annealing in reducing atmospheres introduces oxygen deficiency and increases the DC conductivity, but did not affect the microwave dielectric losses [61].

(7) Losses at high fields were correlated with charge injection across the Schottky barriers, which, in contrast to low field losses, were strongly affected by vacuum anneals. The losses and leakage at high fields could be restored to their as-deposited values by subsequent annealing in air, making oxygen vacancies likely candidates responsible for the lowering of the effective Schottky barrier height.

ACKNOWLEDGMENTS

Support for this research from the DOE Office of Basic Energy Sciences under grant # DE-FG03-02ER45994 is gratefully acknowledged. The authors thank Dr. Tom Mates for help with the SIMS analysis and Dr. Dmitri Klenov for helpful discussions. This work made use of the MRL Central Facilities supported by the National Science Foundation under Award No. DMR 00-80034. S. P. K. was supported by the National Science Foundation IGERT program under Award No. DGE-9987618. Y.-W. O. would like to thank Prof. Tae-Yeon Seong of GIST for his support and the Ministry of Education (Korea) through the Brain Korea 21 project for financial assistance.

REFERENCES

1. A. K. Tagantsev, V. O. Sherman, K. F. Astafiev, J. Venkatesh, and N. Setter, J. Electroceram. **11,** 5 (2003).
2. S. Roberts, Phys. Rev. **71,** 890 (1947).
3. V. L. Gurevich and A. K. Tagantsev, Adv. Phys. **40,** 719 (1991).
4. K. Bethe, *Über das Mikrowellenverhalten nichtlinearer Dielektrika* (Philips Res. Repts. Suppl., 1970).
5. K. Ikuta, Y. Umeda, and Y. Ishi, Jpn. J. Appl. Phys. Part 2 **34** (1995).
6. D. C. Dube, J. Baborowski, P. Muralt, and N. Setter, Appl. Phys. Lett. **74,** 3546 (1999).
7. K. F. Astafiev, V. O. Sherman, A. K. Tagantsev, N. Setter, T. Kaydanova, and D. S. Ginley, Appl. Phys. Lett. **84,** 2385 (2004).
8. O. G. Vendik, L. T. Ter-Martirosyan, and S. P. Zubko, J. Appl. Phys. **84,** 993 (1998).
9. K. A. Muller and H. Burkard, Phys. Rev. B **19,** 3593 (1979).
10. P. A. Fleury, J. F. Scott, and J. M. Worlock, Phys. Rev. Lett. **21,** 16 (1968).
11. R. A. Cowley, Phys. Rev. Lett. **9,** 159 (1962).
12. G. Shirane and Y. Yamada, Phys. Rev. **177,** 858 (1969).
13. T. Sakudo and H. Unoki, Phys. Rev. Lett. **26,** 851 (1971).
14. D. O. Klenov, T. R. Taylor, and S. Stemmer, J. Mater. Res. **19,** 1477 (2004).
15. S. Schmidt, J. W. Lu, S. P. Keane, L. D. Bregante, D. O. Klenov, and S. Stemmer, J. Amer. Ceram. Soc. **88,** 789 (2005).
16. S. Schmidt, Y.-W. Ok, J. W. Lu, D. O. Klenov, S. P. Keane, and S. Stemmer, J. Mater. Res. (submitted) (2005).

17. R. F. C. Farrow, G. R. Harp, R. F. Marks, T. A. Rabedeau, M. F. Toney, D. Weller, and S. S. P. Parkin, J. Cryst. Growth **133,** 47 (1993).

18. T. C. Tisone and J. Drobek, J. Vac. Sci. Technol. **9,** 271 (1971).

19. M. DiBattista and J. W. Schwenk, J. Appl. Phys. **86,** 4902 (1999).

20. G. R. Fox, S. Trolier-McKinstry, S. B. Krupanidhi, and L. M. Casas, J. Mater. Res. **10,** 1508 (1995).

21. C. S. Hwang, M. D. Vaudin, and P. K. Schenck, Journal of Materials Research **13,** 368 (1998).

22. T. Tani, Z. Xu, and D. A. Payne, Mat. Res. Soc. Symp. Proc. **310,** 269 (1993).

23. D. Taylor, J. Br. Ceram. Soc. **84,** 181 (1985).

24. R. S. Krishnan, R. Srivivasan, and S. Devanarayanan, *Thermal expansion of crystals* (Pergamon, New York, 1979).

25. G. W. Dietz and R. Waser, Thin Solid Films **299,** 53 (1997).

26. G. W. Dietz, M. Schumacher, R. Waser, S. K. Streiffer, C. Basceri, and A. I. Kingon, J. Appl. Phys. **82,** 2359 (1997).

27. T. Tamura, K. Takai, H. Noshiro, M. Kimura, S. Otani, and M. Yamada, Jap. J. Appl. Phys. Part 2 **33,** L1697 (1994).

28. S. Zafar, R. E. Jones, B. Jiang, B. White, V. Kaushik, and S. Gillespie, Appl. Phys. Lett. **73,** 3533 (1998).

29. J. D. Baniecki, R. B. Laibowitz, T. M. Shaw, K. L. Saenger, P. R. Duncombe, C. Cabral, D. E. Kotecki, H. Shen, J. Lian, and Q. Y. Ma, J. Europ. Ceram. Soc. **19,** 1457 (1999).

30. P. C. McIntyre, J. H. Ahn, R. J. Becker, R. V. Wang, S. R. Gilbert, L. W. Mirkarimi, and M. T. Schulberg, J. Appl. Phys. **89,** 6378 (2001).

31. Y. Fukuda, K. Numata, K. Aoki, A. Nishimura, G. Fujihashi, S. Okamura, S. Ando, and T. Tsukamoto, Jpn. J. Appl. Phys. Part 2 **37,** L453 (1998).

32. P. C. Chen, H. Miki, Y. Shimamoto, Y. Matsui, M. Hiratani, and Y. Fujisaki, Jpn. J. Appl. Phys. Part 1 **37,** 5112 (1998).

33. P. C. McIntyre, J. Appl. Phys. **89,** 8074 (2001).

34. J. K. Schaeffer, L. R. C. Fonseca, S. B. Samavedam, Y. Liang, P. J. Tobin, and B. E. White, Appl. Phys. Lett. **85,** 1836 (2004).

35. J. P. Han and T. P. Ma, Integr. Ferroelectr. **17,** 471 (1997).

36. R.-V. Wang and P. C. McIntyre, J. Appl. Phys. **94,** 1926 (2003).

37. L. C. Feldman and J. W. Mayer, *Fundamentals of Surface and Thin Film Analysis* (Elsevier Science, New York, 1986).

38. C. Zhou and D. M. Newns, J. Appl. Phys. **82,** 3081 (1997).

39. S. K. Streiffer, C. Basceri, C. B. Parker, S. E. Lash, and A. I. Kingon, J. Appl. Phys. **86,** 4565 (1999).

40. N. A. Pertsev, A. G. Zembilgotov, and A. K. Tagantsev, Phys. Rev. Lett. **80,** 1988 (1998).

41. A. K. Tagantsev, N. A. Pertsev, P. Muralt, and N. Setter, Phys. Rev. B **65,** art. (2002).

42. N. A. Pertsev, A. K. Tagantsev, and N. Setter, Phys. Rev. B **61,** R825 (2000).

43. J. H. Haeni, P. Irvin, W. Chang, R. Uecker, P. Reiche, Y. L. Li, S. Choudhury, W. Tian, M. E. Hawley, B. Craigo, A. K. Tagantsev, X. Q. Pan, S. K. Streiffer, L. Q. Chen, S. W. Kirchoefer, J. Levy, and D. G. Schlom, Nature **430,** 758 (2004).

44. D. Fuchs, C. W. Schneider, R. Schneider, and H. Rietschel, J. Appl. Phys. **85,** 7362 (1999).

45. K. Astafiev, V. Sherman, A. Tagantsev, N. Setter, P. Petrov, T. Kaydanova, D. Ginley, S. Hoffmann-Eifert, U. Bottger, and R. Waser, Integr. Ferroelectr. **58,** 1371 (2003).

46. S. P. Keane, S. Schmidt, J. W. Lu, and S. Stemmer, in preparation.

47. J. Krupka, R. G. Geyer, M. Kuhn, and J. H. Hinken, IEEE Microwave Theory Techn. **42,** 1886 (1994).

48. C. Ang, A. S. Bhalla, R. Guo, and L. E. Cross, Applied Physics Letters **76,** 1929 (2000).

49. A. Eriksson, A. Deleniv, and S. Gevorgian, J. Appl. Phys. **93,** 2848 (2003).

50. S. Saha, D. Y. Kaufman, S. K. Streiffer, and O. Auciello, Appl. Phys. Lett. **83,** 1414 (2003).

51. M. E. Lines and A. M. Glass, *Principles and Applications of Ferroelectric and Related Materials* (Oxford University Press, New York, 2001).

52. R. Viana, P. Lunkenheimer, J. Hemberger, R. Bohmer, and A. Loidl, Phys. Rev. B **50,** 601 (1994).

53. W. T. Chang, J. S. Horwitz, A. C. Carter, J. M. Pond, S. W. Kirchoefer, C. M. Gilmore, and D. B. Chrisey, Appl. Phys. Lett. **74,** 1033 (1999).

54. J. Im, O. Auciello, and S. K. Streiffer, Thin Solid Films **413,** 243 (2002).

55. V. V. Daniel, *Dielectric Relaxation* (Academic Press, London, 1967).

56. Z. Yu, C. Ang, R. Y. Guo, A. S. Bhalla, and L. E. Cross, Appl. Phys. Lett. **80,** 1034 (2002).

57. C. Ang, L. E. Cross, Z. Yu, R. Guo, A. S. Bhalla, and J. H. Hao, Appl. Phys. Lett. **78,** 2754 (2001).

58. X. X. Xi, H. C. Li, W. D. Si, A. A. Sirenko, I. A. Akimov, J. R. Fox, A. M. Clark, and J. H. Hao, J. Electroceram. **4,** 393 (2000).

59. C. Ang, R. Guo, A. S. Bhalla, and L. E. Cross, J. Appl. Phys. **87,** 3937 (2000).

60. O. G. Vendik and L. T. Ter-Martirosyan, J. Appl. Phys. **87,** 1435 (2000).

61. G. Rupprecht and R. O. Bell, Phys. Rev. **1,** 1915 (1962).

Table I: Sputtering deposition parameters

Sputter power	150 Watts
Total gas pressure	25 mTorr
Ar flow	80 sccm
O_2 flow	20 sccm
Substrate surface temperature	~ 700 °C

Table II: Dielectric properties of $SrTiO_3$ films measured at room temperature.

	111 textured film		110/111 textured film	
	□	tan□	□	tan□
As fabricated	290	0.0026	263	0.0016
After 1st anneal (vacuum)	307	0.0029	268	0.0013
After 2nd anneal (air)	311	0.0029	280	0.0017

FIGURE CAPTIONS

Figure 1 (color online)

XRD θ-2θ scans for $SrTiO_3$ films deposited on Pt electrodes with Ti adhesion layers underneath the Pt electrode (bottom) and without Ti adhesion layer (top). S = sapphire, STO = $SrTiO_3$.

Figure 2 (color online)

AFM images of (a) the (110)/(111) oriented $SrTiO_3$ film (on sputtered Pt) and (b) of the (111) oriented film on electron beam evaporated Pt with Ti adhesion layer.

Figure 3 (color online)

Dark field plan-view images obtained from the as-deposited (111) oriented $SrTiO_3$ thin film. Planar defects ("T") are likely twin boundaries. Threading dislocations are found near twin boundaries ("A") and in the grain interiors ("O").

Figure 4 (color online)

Electric field dependence of the dielectric permittivity and losses at room temperature for (a) the (111) oriented film and (b) the (110)/(111) oriented film after different annealing steps.

Figure 5 (color online)

Electric field dependence of the leakage current density and the dielectric losses for the (110)/(111) oriented film after vacuum and a subsequent air anneal, respectively. The inset

shows a Schottky plot with the leakage current density plotted against $E^{0.5}$, yielding a straight line, and which was used to extract the barrier height change.

Figure 6 (color online)

SIMS hydrogen depth profiles across Pt/$SrTiO_3$/Pt capacitors [(110/111) oriented $SrTiO_3$] after annealing in vacuum and subsequent air anneal, respectively. The Pt profile is also shown to identify the layers. The profiles are the sum of five runs.

Figure 7 (color online)

Inverse out-of-plane dielectric susceptibility, $1/\kappa_{33}$, as a function of temperature for the as-deposited (111) oriented $SrTiO_3$ film on the Ti/Pt electrode (filled symbols) and the (110)/(111) oriented $SrTiO_3$ film on the sputtered Pt electrode (open symbols). Lines represent linear fits to the data. For the (111) oriented film, only the data above 150 K was fitted.

Figure 8 (color online)

Dielectric loss tangent under zero applied bias field as a function of temperature measured for the same device, as-fabricated (circles), after vacuum annealing (squares) and after air anneal (triangles) for (a) the (111) oriented film and (b) the (110)/(111) oriented film. Arrows indicate a loss peak around 250 K.

Figure 9 (color online)

Dielectric loss tangent under zero applied bias field as a function of temperature and frequency for the as-deposited (111) oriented film. The lines between the data points serve as a guide to the

eye. The small arrows indicate approximate positions of the maxima of the high-temperature loss peak for the different measurement frequencies.

Figure 10 (color online)

Dielectric loss tangent under an applied bias field of ~ 300 kV/cm as a function of temperature measured for the same device, as-fabricated (circles), after vacuum annealing (squares) and after air anneal (triangles) for (a) the (111) oriented film and (b) the (110)/(111) oriented film. Arrows indicate a loss peak around 250 K.

Figure 11 (color online)

Dielectric loss tangent under an applied bias field of ~ 500 kV/cm as a function of temperature measured for the same device, as-fabricated (circles), after vacuum annealing (squares) and after air anneal (triangles) for (a) the (111) oriented film and (b) the (110)/(111) oriented film. Note the different scale of the loss axis in (b).

Figure 1

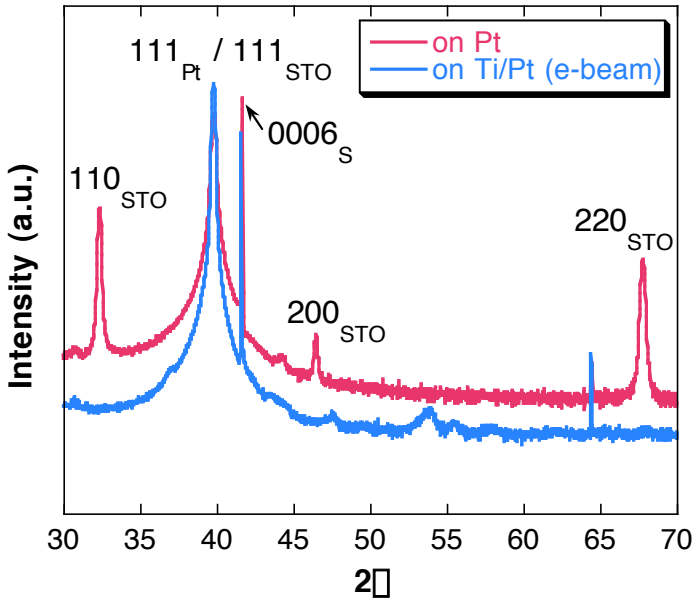
on Pt
on Ti/Pt (e-beam)
111Pt / 111STO
0006S
110STO
220STO
200STO
Intensity (a.u.)
30
35
40
45
50
55
60
65
70
2θ

Figure 2

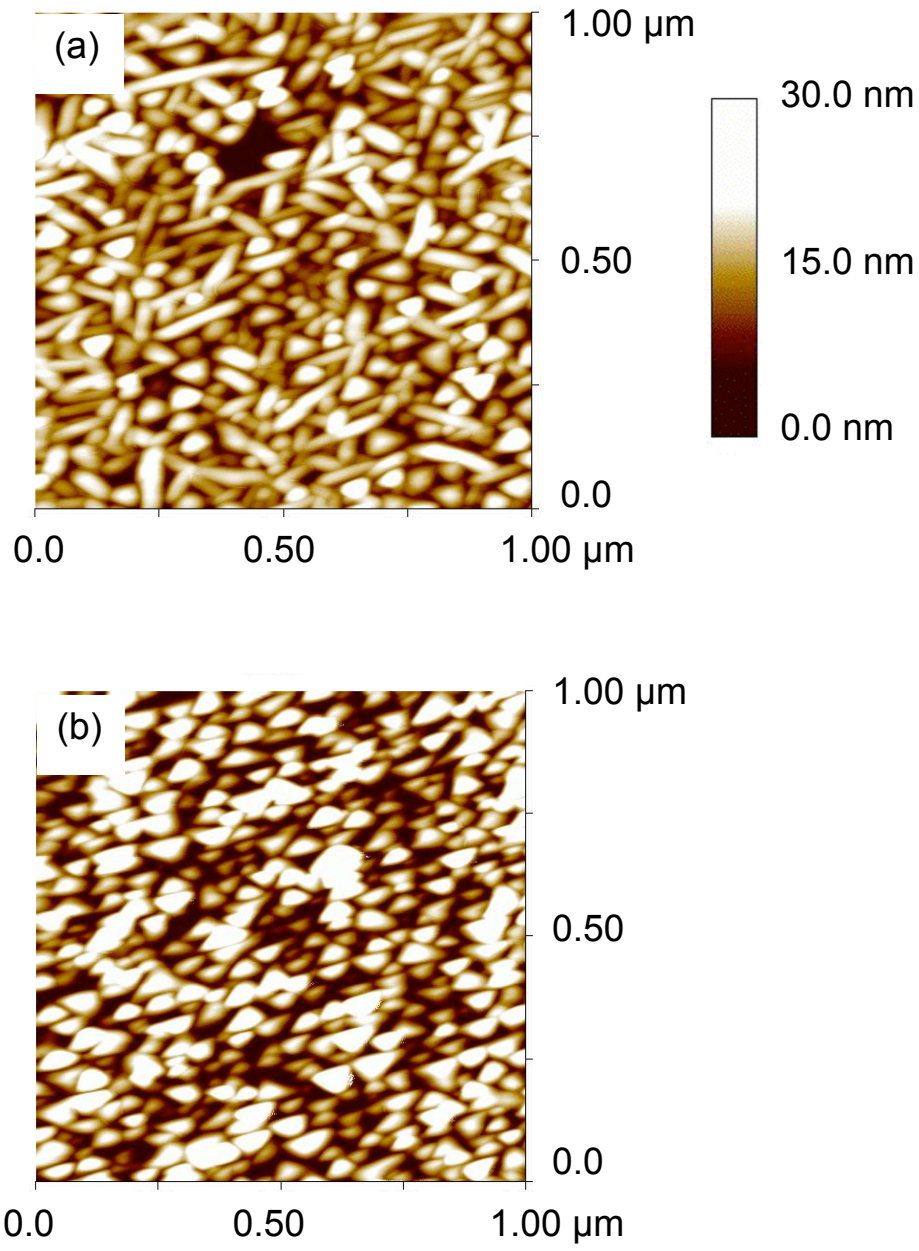
(a)
1.00 µm
0.50
0.0
0.0
0.50
1.00 µm
30.0 nm
15.0 nm
0.0 nm
(b)
1.00 µm
0.50
0.0
0.0
0.50
1.00 µm

Figure 3

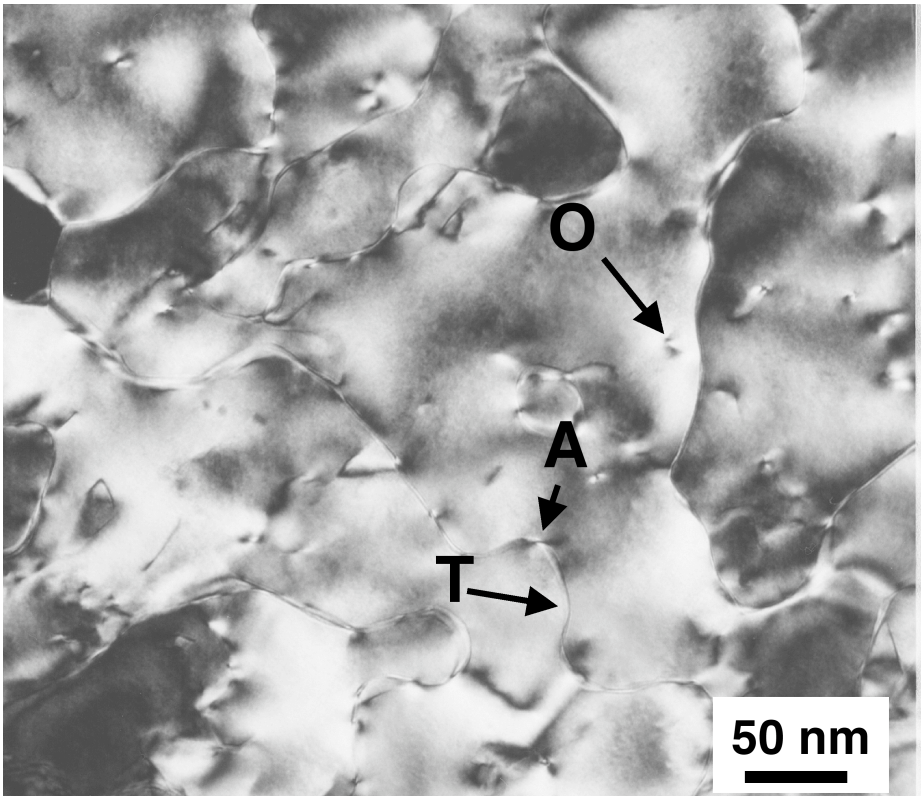

Figure 4

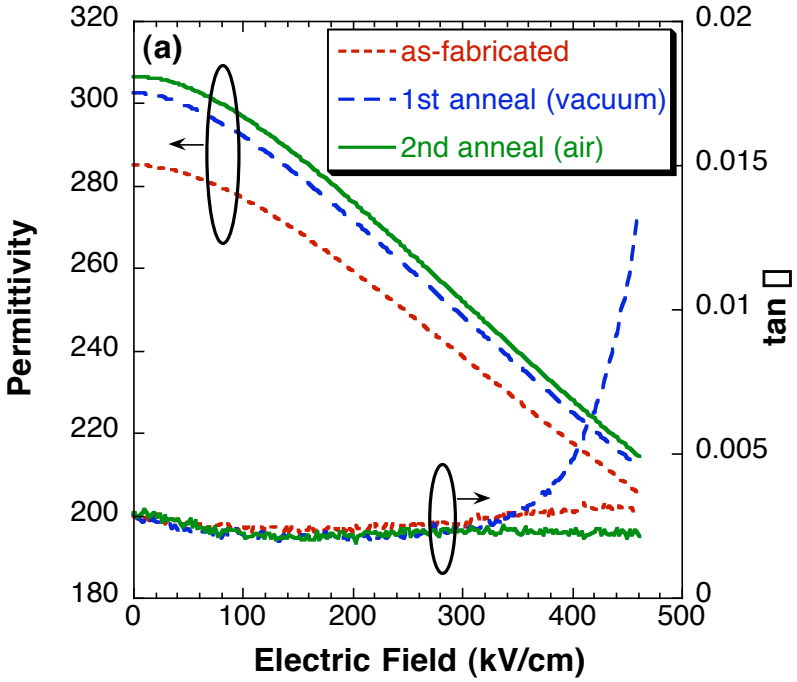
(a)
as-fabricated
1st anneal (vacuum)
2nd anneal (air)
Permittivity
tan □
Electric Field (kV/cm)
320
300
280
260
240
220
200
180
0.02
0.015
0.01
0.005
0
0
100
200
300
400
500

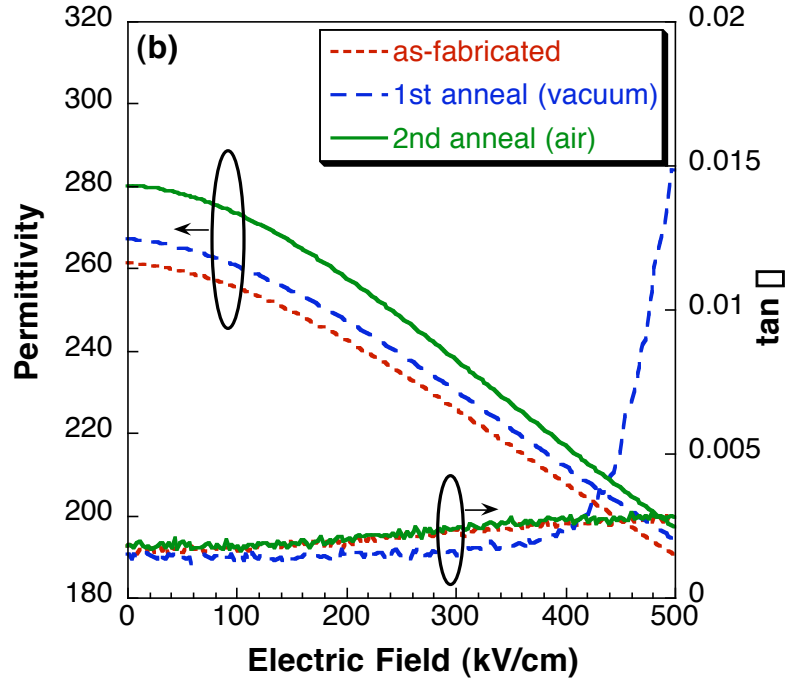
(b)
as-fabricated
1st anneal (vacuum)
2nd anneal (air)
Permittivity
tan □
Electric Field (kV/cm)
320
300
280
260
240
220
200
180
0.02
0.015
0.01
0.005
0
0
100
200
300
400
500

Figure 5

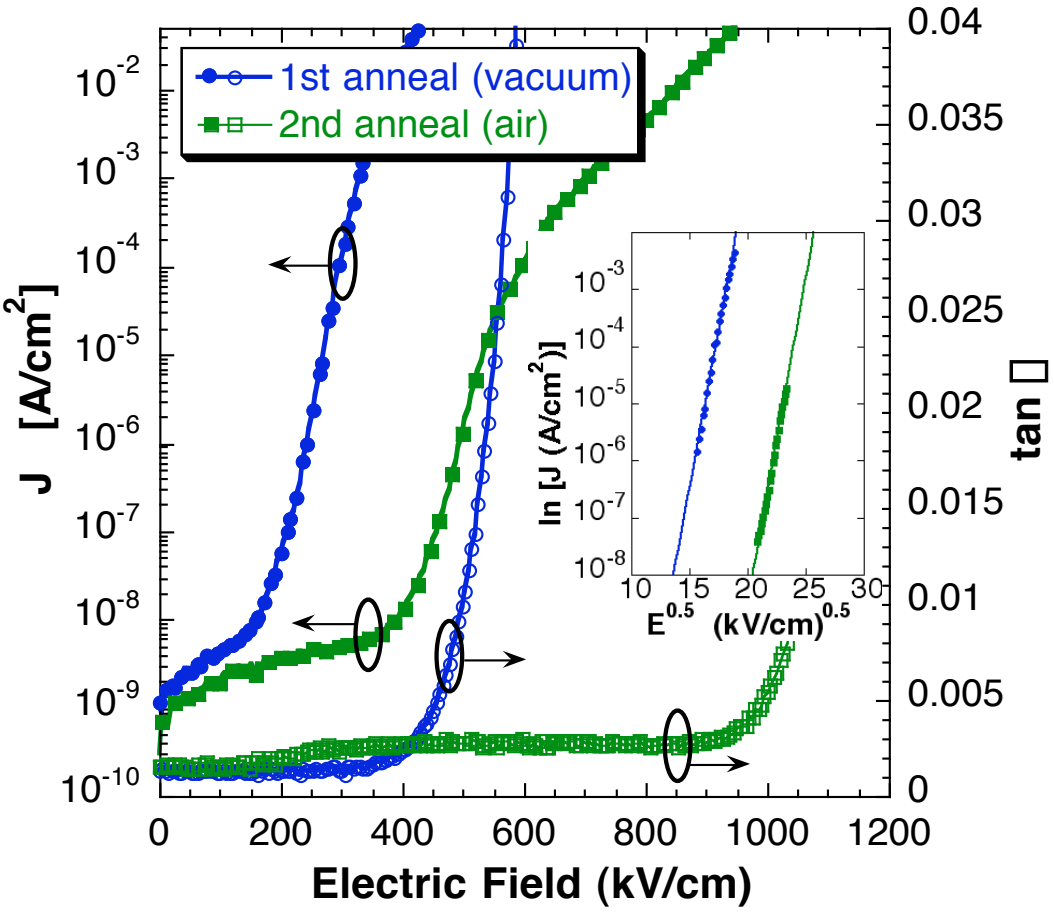
1st anneal (vacuum)
2nd anneal (air)
J [A/cm²]
tan δ
Electric Field (kV/cm)
ln [J (A/cm²)]
E^0.5 (kV/cm)^0.5

Figure 6

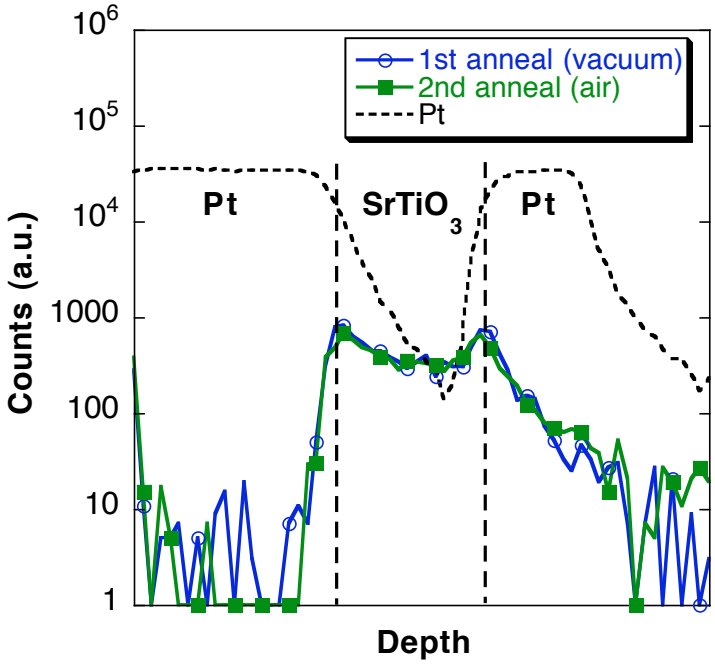
1st anneal (vacuum)
2nd anneal (air)
Pt
Pt
SrTiO3
Pt
Counts (a.u.)
Depth
10^6
10^5
10^4
1000
100
10
1

Figure 7

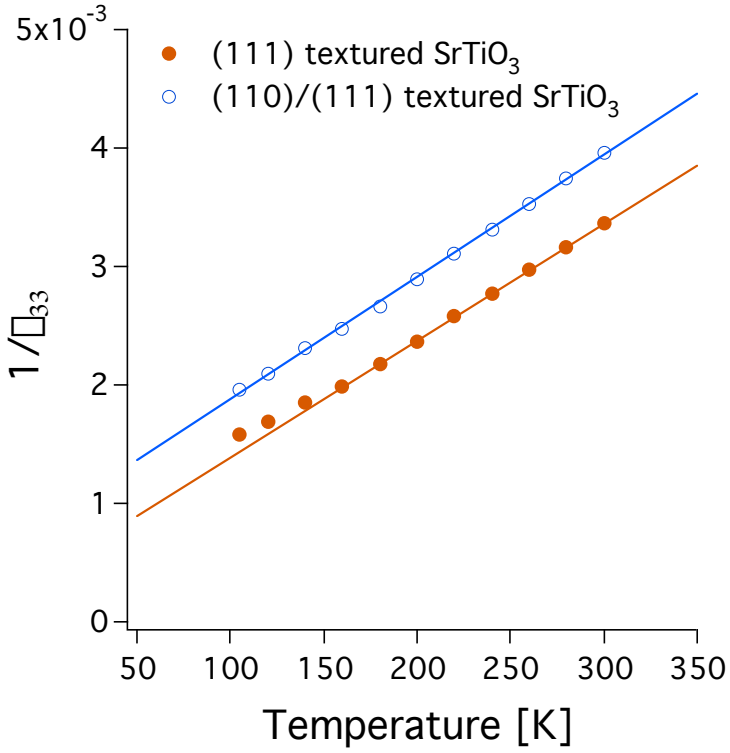
5x10-3
(111) textured SrTiO3
(110)/(111) textured SrTiO3
4
3
2
1
0
1/□33
50
100
150
200
250
300
350
Temperature [K]

Figure 8

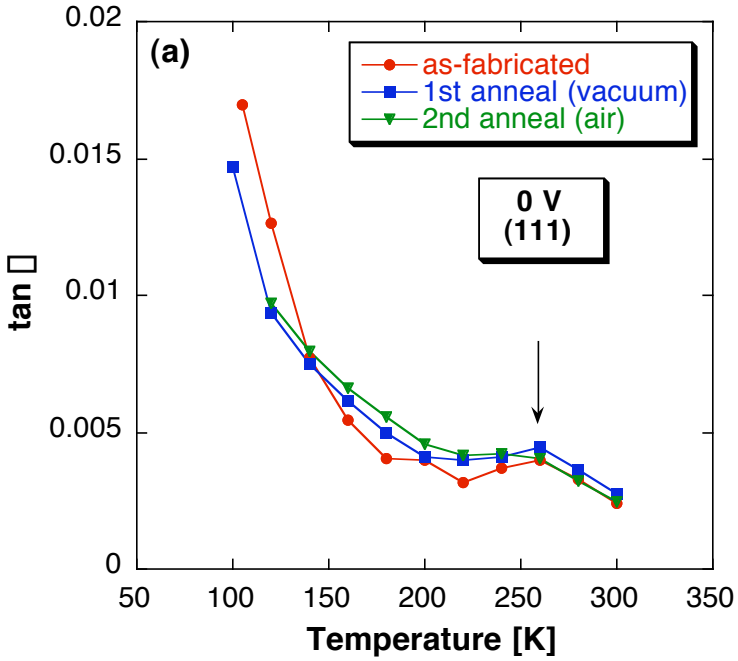
(a)
as-fabricated
1st anneal (vacuum)
2nd anneal (air)
0 V
(111)
tan □
0.02
0.015
0.01
0.005
0
50
100
150
200
250
300
350
Temperature [K]

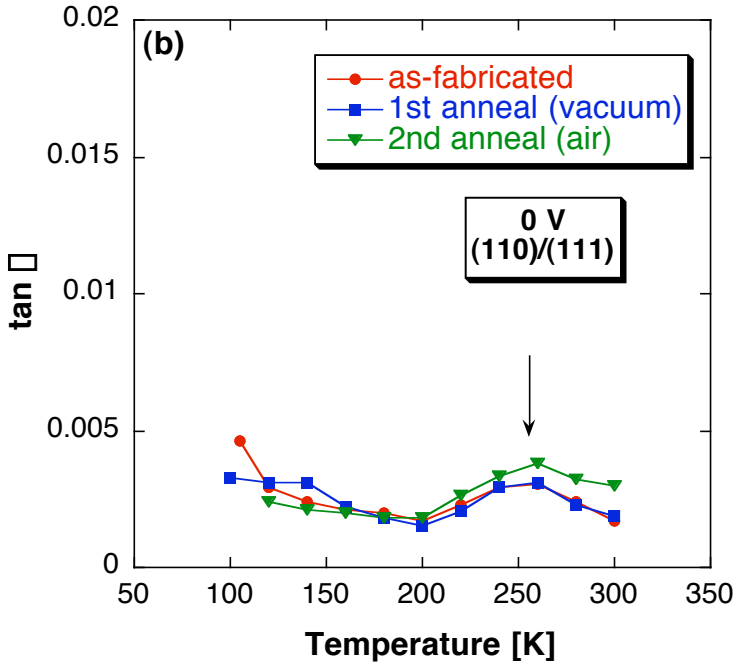
(b)
as-fabricated
1st anneal (vacuum)
2nd anneal (air)
0 V
(110)/(111)
tan □
0.02
0.015
0.01
0.005
0
50
100
150
200
250
300
350
Temperature [K]

Figure 9

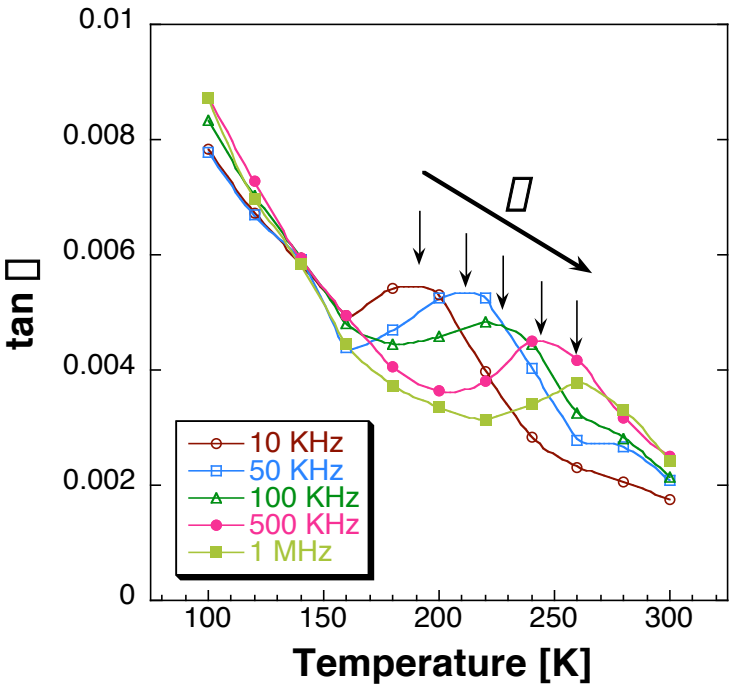
0.01
0.008
0.006
0.004
0.002
0
tan □
100
150
200
250
300
Temperature [K]
10 KHz
50 KHz
100 KHz
500 KHz
1 MHz
□

Figure 10

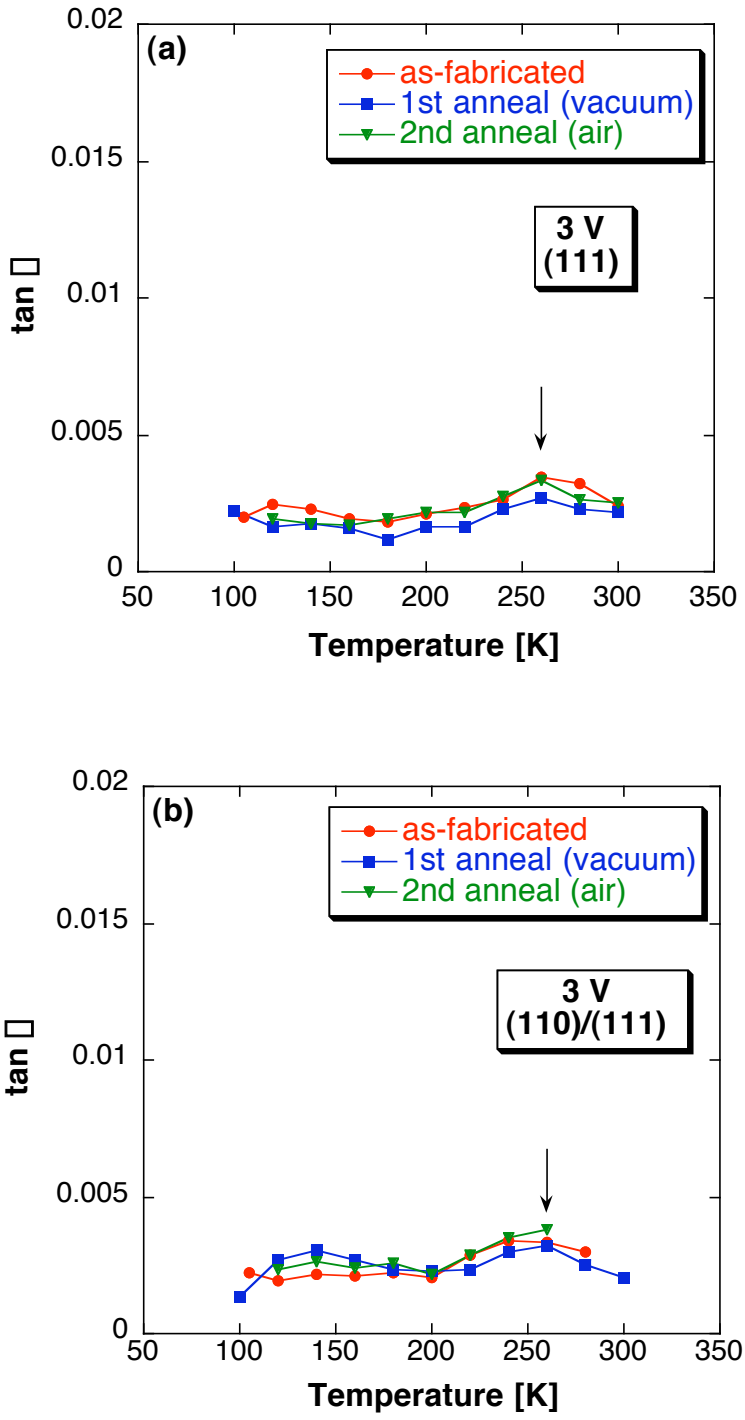
(a)
as-fabricated
1st anneal (vacuum)
2nd anneal (air)
3 V
(111)
tan □
0.02
0.015
0.01
0.005
0
50
100
150
200
250
300
350
Temperature [K]
(b)
as-fabricated
1st anneal (vacuum)
2nd anneal (air)
3 V
(110)/(111)
tan □
0.02
0.015
0.01
0.005
0
50
100
150
200
250
300
350
Temperature [K]

Figure 11

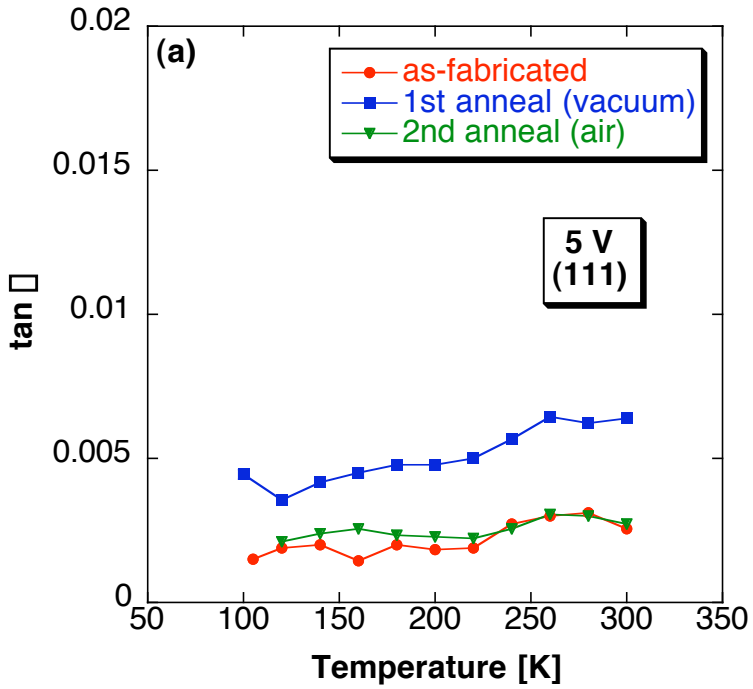
(a)
as-fabricated
1st anneal (vacuum)
2nd anneal (air)
5 V
(111)
tan □
0.02
0.015
0.01
0.005
0
50
100
150
200
250
300
350
Temperature [K]

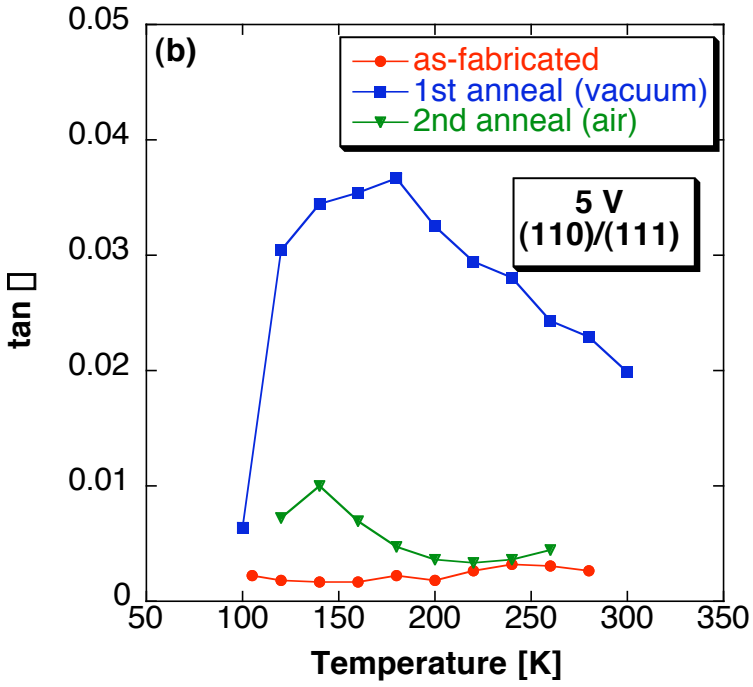
(b)
as-fabricated
1st anneal (vacuum)
2nd anneal (air)
5 V
(110)/(111)
tan □
0.05
0.04
0.03
0.02
0.01
0
50
100
150
200
250
300
350
Temperature [K]